

On the capability of high redshift kSZ measurement with galaxy surveys

Ziyang Chen^{a,b} Pengjie Zhang^{a,c,b}

^aDepartment of Astronomy, School of Physics and Astronomy, Shanghai Jiao Tong University, Shanghai, China

^bKey Laboratory for Particle Astrophysics and Cosmology (MOE)/Shanghai Key Laboratory for Particle Physics and Cosmology, Shanghai, China

^cTsung-Dao Lee Institute, Shanghai Jiao Tong University, Shanghai 200240, China

E-mail: chen_zy@sjtu.edu.cn; zhangpj@sjtu.edu.cn

Abstract. The kinematic Sunyaev-Zel'dovich (kSZ) effect has been detected at $z < 1$ using various techniques and data sets. The ongoing and upcoming spectroscopic galaxy surveys such as DESI (Dark Energy Spectroscopic Instrument) and PFS (Prime Focus Spectrograph) will push the detection beyond $z = 1$, and therefore map the baryon distribution at high redshifts. Such detection can be achieved by both the kSZ stacking and tomography methods. While the two methods are theoretically equivalent, they differ significantly in the probed physics and scales, and required data sets. Taking the combination of PFS and ACT (Atacama Cosmology Telescope) as an example, we build mocks of kSZ and galaxies, quantify the kSZ detection S/N, and compare between the two methods. We segment the PFS galaxies into three redshift bins: $0.6 < z < 1.0$, $1.0 < z < 1.6$, and $1.6 < z < 2.4$. For tomography method, our analysis reveals that the two higher redshift bins exhibit significantly higher S/N ratios, with values of 32 and 28, respectively, compared to the first redshift bin, which yielded an S/N of 8. This is attributed to not only the increasing of electron density with redshifts, but also the larger survey volume and the reduced non-linearity, facilitating velocity reconstruction at higher redshifts. Therefore, the capability of the PFS survey to measure high redshift kSZ effect stands as a substantial advantage over other spectroscopic surveys at lower redshift. The S/N of kSZ stacking largely depends on the number of clusters/groups available from another photometric survey. But in general, its S/N is lower than that of kSZ tomography, largely due to CMB instrument noise and error in cluster redshift. Incorporating next-generation CMB surveys like CMB-S4, characterized by significantly reduced instrument noise and improved angular resolution, is expected to enhance tomographic detection by a factor of ten and stacking detection by fivefold. This future high S/N detection holds the promise of not only providing precise constraints on the overall baryon abundance but also initiating a new insight into baryon distribution.

Keywords: Sunyaev-Zeldovich effect; cosmological parameters from LSS

Contents

1	Introduction	1
2	Velocity reconstruction method	3
3	Mock generation	5
3.1	CosmicGrowth	5
3.2	Mock kSZ/CMB maps	6
3.3	Mock galaxy, cluster catalogs	8
4	Forecast kSZ measurements with PFS survey	8
4.1	Stacking method	9
4.2	Tomography method	12
5	Conclusion	14
A	The difference between dark matter and baryon	15
B	Connection between halos and galaxies	16
C	The equivalence between kSZ measurement methods	17
D	Test the velocity reconstruction method	19

1 Introduction

In cosmology, the kinematic Sunyaev Zel'dovich (kSZ) effect stands as a pivotal probe for understanding the large-scale baryon distribution of the universe. The kSZ effect, a secondary anisotropy in the CMB, arises from the inverse Compton scattering of CMB photons off a group of free electrons moving with respect to the CMB rest frame. Unlike the thermal Sunyaev-Zel'dovich (tSZ) effect and X-ray emissions, the kSZ effect linearly depends on electron density and is independent of electron temperature, making it a valuable probe for mapping baryon in less dense regions of the universe, such as filaments and voids. This probe has powerful constraining ability in colder and the context of "missing baryon" problem in the local universe, where observations [1] suggest a 50% deficit relative to the predictions of Big Bang Nucleosynthesis (BBN) [2]. On the other hand, if the baryon distribution can be constraint by other observations, such as tSZ [3], Fast Radio Bursts [4], the kSZ effect encodes valuable information about the growth rate [5, 6] of the universe's matter content, leveraging the investigation of the dark energy [7], modified gravity [8–10] and neutrino mass [11].

Despite its significance, the kSZ signal is notably faint compared to other CMB components, presenting a formidable challenge for accurate detection and measurement. A critical aspect of extracting the kSZ signal hinges on its unique dependence on the peculiar velocity field. The first measurement of the kSZ effect by ref. [12] utilized the pairwise method, which capitalizes on the gravitational interaction between cluster pairs moving towards each other. While this method provides insights into the relative motion between clusters, it overlooks

the collective motion that could yield additional information. Refs. [13–16] further developed this method and gain $1.8 \sim 5.4\sigma$ detection. The advantage of the pairwise method is not requiring precise knowledge of the clusters’ peculiar velocities and can utilize enormous number of photo-z groups [17–20].

Advancing the measurement of the kSZ effect involves reconstructing peculiar velocities of clusters, from spectroscopic redshift galaxy surveys [21–24]. By stacking the CMB signals at cluster locations, the signal-to-noise ratio (S/N) is enhanced. And weighting them by the line-of-sight (LOS) velocities would effectively isolate the kSZ signal from other unrelated CMB components. This approach is particularly effective in studying baryon distributions around clusters. Refs. [25, 26] investigated the effect of various factors on reconstruction efficiency, such as RSD, photometric redshift errors, satellite galaxy fraction, the adoption of incorrect cosmological models, and the scale of smoothing. In addition, they applied this method to a realistic mock, include light cone effect, survey masks and selection functions. In addition, ref. [27] attempted to reconstruct velocity by Convolutional Neural Network and find performance is slightly improved comparing to the conventional method which uses the continuity equation [28].

The above kSZ stacking method requires pre-existing cluster/group catalogs, other than the spectroscopic redshift galaxy catalogs. Alternatively, the kSZ tomography method, as proposed by ref. [29, 30], requires no such cluster/group catalog. It reconstructs a kSZ template, which integrates the reconstructed momentum field $\hat{\mathbf{p}} = (1 + \hat{\delta})\hat{\mathbf{v}}$ along the LOS with a weight dependent on redshift as an estimator of the true kSZ signal. This estimator, uncorrelated with other CMB components, extracts the kSZ signal by correlating with a CMB map. This technique is adept at assessing the kSZ effect on the large scale, sensitive to baryon distributions in not only clusters/groups, but also filaments and even voids.

Existing kSZ measurements have provided useful information on the baryon distribution and evolution in our universe. Ref. [13] sought to quantify the baryon abundance around central galaxies at redshift $z \sim 0.1$ by estimating the pairwise signal using the combination of Planck data and the a Central Galaxy Catalogue samples from the SDSS-DR7. Further refining this measurement, ref. [31] constrained on the baryon fraction by increasing the aperture filter radius and reported an increment in the baryon fraction to 45-55% of the total baryonic content when the filter radius equals to 10 arcmin, albeit with an increasing noise at larger radii. Ref. [32] extended the detection of baryon fraction to higher redshift ($z = 0.4$), cross-correlating between a projected density field and the squared CMB temperature map. This work achieved a 4.5σ confirmation that the baryon fraction aligns with BBN prediction. The study continued by ref. [33], which applied a similar methodology across three unWISE galaxy catalog samples peaking at redshifts of 0.6, 1.1, and 1.5. Their results indicated the free gas fraction for the higher redshift bins is about twice higher than the fiducial value. They attributed the abnormally high kSZ signal amplitude to uncertainties in theoretical modeling. In addition, by measuring the pairwise kSZ signal of clusters in redshift span $0.1 \sim 0.9$, ref. [17] constrained the gas fraction $f_{\text{gas}} = 0.086 \pm 0.027$ inside the R_{500} . Measuring the pairwise kSZ in Fourier space, ref. [34] constrained the gas fraction of LOWZ catalog from BOSS DR12, $f_{\text{gas}} = 0.17$, while this result has large error contour and has a degeneracy with the assumption of gas profiles. Ref. [35] extracted the kSZ signal of a group catalog from SDSS DR7 [36] and Planck. They divided the catalog into six mass bins and measure the kSZ flux inside R_{200} as a function of halo mass. They found the relationship of kSZ flux and halo mass is self-similar, inferring a mass-independent baryon fraction. They also found the baryon fraction of all mass bin is consistent with the universal value within

the errorbars and indicate all “missing baryons” are found on the halo scales. The discussing of “missing baryon” problem has been last twenty years and hasn’t been settled down due to current low measurement significance. Refs. [23, 24, 37] concentrated more on the baryon distribution inside the groups, thanks to the high resolution of ACT survey. They measured the gas density profile by stacking the kSZ signal at the position of a photometric cluster catalog with varying filter size to extract kSZ signal from CMB maps, weighting with the line-of-sight (LOS) velocity reconstructed by another spectroscopic galaxy catalog. They found the gas profile is more extended than that of dark matter and point out the potential of kSZ effect to measuring the feedback in the galaxy formation model [38].

Detection of kSZ through galaxy-CMB cross-correlation so far is limited to $z < 1$. Ongoing surveys such as DESI and Euclid and upcoming surveys such as PFS will push the measurement to $z > 1$ and reveal the baryons at high redshifts. The capability of kSZ measurement at high redshift is promising due to higher electron number density and potentially better velocity reconstruction. In this study, we forecast the measurement significance of kSZ using the PFS and the CMB surveys such as ACT and CMB-S4. Because PFS provides accurate positions of galaxies with spectroscopic redshifts, which can facilitate the velocity reconstruction, we focus on stacking and tomography methods. These two methods offer complementary insights, measuring the one-halo and two-halo terms of the kSZ signal, respectively. The PFS extends to redshifts of $z = 2.4$, enabling high-redshift measurements. Such high-redshift observations can constrain the abundance and evolution of baryons, providing valuable insight in the ‘missing baryon’ problem. Moreover, one-halo term measurements of the kSZ effect could reveal the baryon fraction in clusters as a function of radius, which is sensitive to baryonic processes such as supernova and Active Galactic Nuclei (AGN) feedback, aiding in calibrating hydrodynamic simulations. As ref. [39] demonstrates, simulations with varying galaxy formation models align at lower redshifts but diverge significantly beyond $z = 2$. Thus, high-redshift kSZ measurements offer invaluable information for understanding the galaxy formation model.

This paper is organized as follows. In section 2, we present the velocity reconstruction algorithm used in both stacking and tomography methods. In section 3 we introduce the N-body simulation CosmicGrowth and the methods to construct the mock galaxy/cluster catalogs and kSZ/CMB maps. Then we show the forecast of the kSZ measurement significance with two method in section 4. In the end, we conclude in section 5.

2 Velocity reconstruction method

To extract the kSZ signal from other CMB components, the key is to leverage its correlation with the peculiar velocity of the electron bulk, which is absent in other components. Both kSZ stacking and tomography measurement methods involve reconstructing the peculiar velocity field. In this section, we describe the method of velocity reconstruction from a spectroscopic redshift galaxy catalog.

In the linear regime, the large-scale velocity field is determined by the density field through the continuity equation

$$\dot{\delta}_m + \nabla \cdot \mathbf{v} = 0, \quad (2.1)$$

where δ_m is the matter overdensity and \mathbf{v} is the peculiar velocity. Furthermore, the time derivative of the matter overdensity is expressed as

$$\dot{\delta}_m = \frac{d\delta_m}{da} \dot{a} = H f \delta_m, \quad (2.2)$$

where $f = d \ln D / d \ln a$ is the growth rate and H is the Hubble parameter. In Fourier space, eq. 2.1 transforms to

$$\hat{\mathbf{v}}(\mathbf{k}) = -i f H \delta_m(\mathbf{k}) \frac{\mathbf{k}}{k^2}, \quad (2.3)$$

where $k = |\mathbf{k}|$ is the length of the wavenumber. In reality, however, the overdensity of dark matter is unknowable. The galaxy overdensity is used as a biased tracer of dark matter, $\delta_g = b_g \delta_m$. Unfortunately, the RSD and shot noise in the galaxy density field would decrease the velocity reconstruction performance. In the following, we use Wiener filters to suppress the noise and optimize the velocity reconstruction.

Our algorithm for reconstructing the velocity field proceeds as follows:

1. Divide the entire simulation volume into 2048^3 voxels, and estimate the overdensity field $\delta_g^{\text{RSD}}(\mathbf{x})$ from the galaxy catalog with the Nearest Grid Point (NGP) method.
2. Estimate the divergence of the velocity $\theta(\mathbf{x}) \equiv \nabla \cdot \mathbf{v}(\mathbf{x})$ from the density field $\delta_g^{\text{RSD}}(\mathbf{x})$ with a Wiener filter defined as

$$W_1(k_\perp, k_\parallel) = \frac{P_{\theta^t, \delta_g^{\text{RSD}}}(k_\perp, k_\parallel)}{P_{\delta_g^{\text{RSD}}, \delta_g^{\text{RSD}}}(k_\perp, k_\parallel)}. \quad (2.4)$$

Here, θ^t represents the true convergence component from the dark matter particles in simulation without RSD, k_\perp is the length of the wavenumber perpendicular to the LOS direction, and k_\parallel the length is the parallel component. This Wiener filter $W_1(k_\perp, k_\parallel)$ is a function dependent on the lengths of k_\perp and k_\parallel . This filter could be derived from simulations incorporating appropriate cosmological and galaxy formation models. And reconstructed convergence component is

$$\hat{\theta}(k_\perp, k_\parallel) = H(z) f(z) W_1(k_\perp, k_\parallel) \delta_g^{\text{RSD}}, \quad (2.5)$$

where $H(z)$, $f(z)$ is the Hubble parameter and growth factor at the effective redshift of the galaxies.

3. Estimate the reconstructed velocity field from the reconstructed convergence component $\hat{\theta}(k_\perp, k_\parallel)$

$$\hat{\mathbf{v}}(k_\perp, k_\parallel) = \frac{-i \mathbf{k}}{|\mathbf{k}|^2} \hat{\theta}(k_\perp, k_\parallel) \quad (2.6)$$

And transform it into the Cartesian coordinates $\hat{\mathbf{v}}(\mathbf{x})$.

In the stacking method, we obtain the LOS velocity of each cluster $\hat{v}_{\text{los},i}$, by interpolating the reconstructed field $\hat{\mathbf{v}}(\mathbf{x})$ at their position $\mathbf{x}_{i,\text{cluster}}^{\text{ph}}$.

In the tomography method, the reconstructed momentum field is the product of the reconstructed density and the reconstructed velocity field

$$\hat{\mathbf{p}}(\mathbf{x}) = (1 + \hat{\delta}(\mathbf{x})) \hat{\mathbf{v}}(\mathbf{x}), \quad (2.7)$$

	Redshift bin	$\bar{n}_g \times 10^{-4} [\text{Mpc}/h]^{-3}$	$V_{\text{survey}} [\text{Gpc}/h]^3$	Snapshot	HOD model
1	$0.6 < z < 1.0$	4	1.38	2746 ($z = 0.811$)	DESI ELG [41]
2	$1.0 < z < 1.6$	6	3.24	2181 ($z = 1.272$)	HSC NB816 [10]
3	$1.6 < z < 2.4$	3	5.29	1631 ($z = 2.023$)	HSC NB912 [10]

Table 1. The detailed information of the three redshift bins. The first column shows the redshift range; the second column shows the mean galaxy number density in this redshift range according to PFS survey; the third column show the comoving volume of the redshift bin; the fourth column shows the snapshot in the CosmicGrowth simulation used to conduct the mock kSZ map, galaxy and cluster catalogs in the redshift bin; the fifth column show the HOD model used to generate the ELGs.

where $\hat{\delta}(\mathbf{k}) = W_2(k)\delta_g^{\text{RSD}}$. $W_2(k)$ is the Wiener filter defined as

$$W_2(k) = \frac{b_g^2 P_{\text{mm}}(k)}{b_g^2 P_{\text{mm}}(k) + \frac{1}{\bar{n}_g}}, \quad (2.8)$$

where $P_{\text{mm}}(k)$ is the matter power spectrum and \bar{n}_g is the mean galaxy number density.

The two Wiener filters, $W_1(k_{\perp}, k_{\parallel})$ and $W_2(k)$, used to mitigate the noise from RSD and shot noise, have been demonstrated theoretically to be the optimal choice in appendix C. And comparing to conventional Gaussian filter, the Wiener filters can improve the tomography method when $k > 0.1h/\text{Mpc}$ (appendix D).

3 Mock generation

The PFS is a cosmology survey that offers unique capabilities in astronomical observations due to its large field of view and impressive multiplexing capability, which enables high sampling rates and coverage of a large volume of space [40]. It is designed to explore a previously uncharted epoch in cosmic history, extend to redshift $z = 2.4$. The sky coverage is 1400 deg^2 . Notably, the PFS survey can cover a comoving volume that is ten times larger than SDSS and twice as large as BOSS, which allows for more detailed studies of cosmic structures and the dark energy component of the universe. The PFS targets a range of galaxy types using optical and near-infrared wavelengths. Specifically, [O II] emission-line galaxies (ELGs), which are useful tracers for conducting an efficient survey out to high redshifts beyond $z=1$.

In this study, we investigate the potential for detecting the kSZ effect with the PFS ELG catalog. We divide the whole redshift range covered by PFS into three bins: $0.6 < z < 1.0$, $1.0 < z < 1.6$ and $1.6 < z < 2.4$. The comoving intervals of these three bins are almost equivalent. The parameters for the PFS cosmology survey for these three bins are listed in table 1. In this section, we describe the generation of mock kSZ maps, PFS galaxy catalogs and cluster catalogs from the CosmicGrowth simulation used to forecast the kSZ measurement significance.

3.1 CosmicGrowth

The CosmicGrowth simulations [42] are a series of high-resolution N-body cosmological simulations designed primarily to study the acceleration of cosmic expansion and the clustering of dark matter and galaxies. The simulations are evolved with an adaptive parallel P3M -body code, while the force between the particles is softened at small scale. In this work, we choose

to use the “WMAP_3072.1200” simulation, whose box length is 1200 Mpc/ h . This simulation adopts a Λ CDM cosmological model with the cosmological parameters from WMAP satellite, $\Omega_b = 0.0445$, $\Omega_c = 0.2235$, $\Omega_\Lambda = 0.732$, $h = 0.71$, $n_s = 0.968$ and $\sigma_8 = 0.83$. It employs 3072^3 dark matter particles. The dark matter groups are identified by the Friends-of-Friends algorithm and the linking length is set to be 0.2 times the mean particle separation. A FoF group catalog is constructed for each snapshot, providing group mass, positions and peculiar velocities. Specifically, we use the snapshots 2746 ($z = 0.811$), 2181 ($z = 1.272$) and 1631 ($z = 2.023$) to generate mock kSZ map, galaxy and cluster catalogs in the three redshift bins.

3.2 Mock kSZ/CMB maps

The amplitude of the kSZ effect between redshift z_1 and z_2 is the integrated momentum of electrons along the LOS direction

$$\frac{\Delta T_{\text{kSZ}}}{T_{\text{CMB}}} = \int_{z_1}^{z_2} \chi_e \bar{n}_e(z) \sigma_T \frac{(1 + \delta_e) \mathbf{v} \cdot \hat{n}}{c} e^{-\tau(z)} ad\chi, \quad (3.1)$$

where χ_e is the ionized baryon fraction, $\bar{n}_e(z)$ is the mean electron density, σ_T is the Thomson scattering cross-section, δ_e and \mathbf{v} is the over-density and peculiar velocity of electron, \hat{n} is the LOS direction, c is the speed of light, $\tau(z) = \int_0^z \chi_e \bar{n}_e(z) \sigma_T ad\chi$ is the Thompson optical depth and χ is the comoving distance. We adopt $\chi_e = 1$, postulating complete ionization within our redshift interval of interest. We further posit that the distribution and velocity of electrons follow those of dark matter, $\delta_e = \delta_{\text{dm}}$ and $\mathbf{v}_e = \mathbf{v}_{\text{dm}}$. While the baryonic processes would cause the divergence between free electrons and dark matter, we discuss in appendix A that this divergence is mostly diminished at large scale and may not cause a notable impact to our conclusion. With the position and velocity of dark matter particles from the simulation, we assign the momentum $\mathbf{p} \equiv (1 + \delta_{\text{dm}}) \mathbf{v}_{\text{dm}}$ to the GRID³ meshes. In this work, we set GRID = 2048. By choosing an arbitrary LOS direction and integrating along this vector under the flat-sky approximation, we synthesize a simulated kSZ map. The redshift evolution in one redshift bin has not been considered here.

To construct maps for the primary CMB and the instrument noise, we utilize their angular power spectrum. First, we establish a same two-dimensional gridding with that of the kSZ map in Fourier space. Each point in this Fourier grid is endowed with a complex amplitude of the square root of the angular power spectrum $\sqrt{C_{l,X}}$, X symbolizing either the CMB or noise, and is complemented by a randomly assigned phase. Transforming the map from Fourier space to real space, a map of temperature fluctuations is achieved. Employing the CAMB software [43], we simulate the primary CMB angular power spectrum, while the noise power spectrum is generated based on the instrumental white noise level Δ_T

$$C_l^{\text{Noise}} = \left(\frac{\Delta_T}{T_{\text{CMB}}} \right)^2. \quad (3.2)$$

In addition we add a beam function

$$W_{\text{beam}}(l) = \exp(-l(l+1)/l_{\text{beam}}^2/2) \quad (3.3)$$

where $l_{\text{beam}} = \sqrt{8 \ln 2} / \theta_{\text{FWHM}}$ and θ_{FWHM} is the beam size, to all three components; kSZ effect, primary CMB and instrument noise. The CMB instrument noise parameters are set to $\Delta_T = 11 \mu\text{K} - \text{arcmin}$, $\theta_{\text{FWHM}} = 1.26 \text{arcmin}$ for ACT case and $\Delta_T = 1 \mu\text{K} - \text{arcmin}$, $\theta_{\text{FWHM}} = 1 \text{arcmin}$ for CMB-S4 case. In top panels of figure 1, we illustrate the mock kSZ

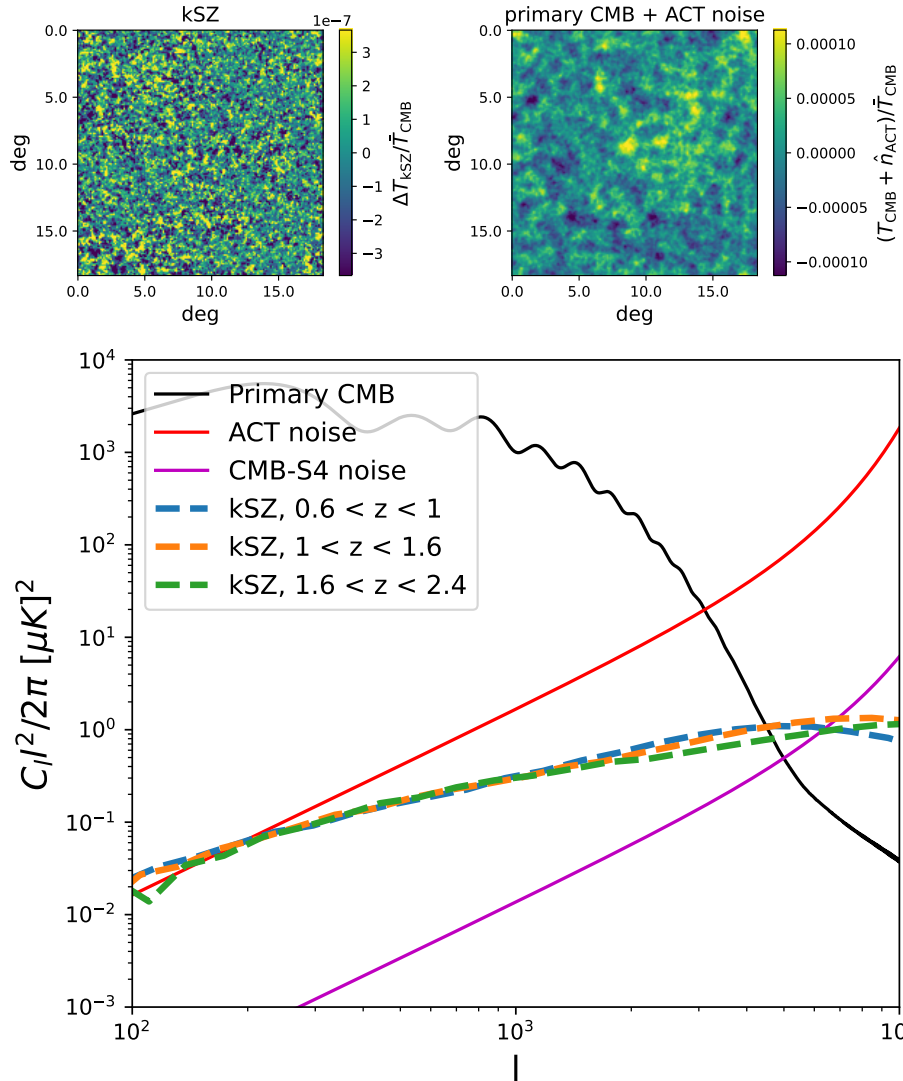


Figure 1. The top two panels show the mock sky map of the kSZ in redshift range $1.6 < z < 2.4$ (top left) and primary CMB with ACT noise (top right). The bottom panel shows the angular power spectrum of primary CMB (black), the instrument noise of ACT (red) and CMB-S4 (pink) and the angular power spectrum of the kSZ between $0.6 < z < 1$, $1 < z < 1.6$, $1.6 < z < 2.4$ (dashed lines).

and the primary CMB plus ACT instrumental noise map, to show the relative scale and amplitude of kSZ effect and its measurement noise, in the redshift interval $1.6 < z < 2.4$ as an example. The bottom panel shows the angular power spectra of kSZ effect in three redshift bins, $0.6 < z < 1.0$, $1.0 < z < 1.6$, $1.6 < z < 2.4$, primary CMB and the instrument noise for both ACT and the upcoming CMB-S4 experiment ($C_l^{\text{Noise}}/W_{\text{beam}}^2(l)$). Notably, the amplitude of the kSZ effect appears lower than the combined intensity of the CMB and noise, by more than two orders of magnitude. This underscores the challenge of distinguishing the kSZ signal against the background of primary CMB fluctuations and instrumental noise, emphasizing the need for robust techniques to extract and interpret the kSZ signal accurately.

3.3 Mock galaxy, cluster catalogs

We generate the galaxy catalog from the FOF group catalog from the simulation and the ELG HOD. In this work we focus on the redshift range $0.6 < z < 2.4$. The redshift range is divided into three redshift bins, $0.6 < z < 1$, $1 < z < 1.6$, $1.6 < z < 2.4$, of which we use different ELG HODs (the details is shown in appendix B). To generate the galaxy catalog mock, we use the following steps:

- Using the HOD to determine whether there is a central galaxy and how many satellite galaxies in each dark matter halo and generating a galaxy catalog.
- Randomly choosing galaxies to make number density of the catalog consistent with the value from PFS science strategy paper (list in table 1).
- Giving the galaxies the same position and peculiar velocity as their host halo. Here, we ignore the relative distance and velocity between a galaxies and its host halo.
- Assigning the RSD to LOS direction position of galaxies.

We use this spectroscopic redshift galaxy mock catalog to reconstruct velocity with the method presented in section. 2.

For the cluster catalog, we use the halos from the simulation whose mass is above a specific mass limitation. The photometric redshift uncertainty is assigned by $\sigma_z = 0.01(1+z)$. We use this cluster catalog to determine where to stacking the filtered CMB temperature. This cluster sample is assumed to be identified from photometric galaxies using a group finder such as ref. [36]. The clusters can point out the positions where is abundant of free electron and improve the measurement significance.

4 Forecast kSZ measurements with PFS survey

In this section, we explore the efficacy of the stacking and tomography methods by assessing the kSZ effect measurement significance, utilizing the PFS survey. Both methods incorporate a crucial step, the reconstruction of velocity, that significantly impacts measurement accuracy. To quantify the performance of the velocity reconstruction, we employ the correlation function

$$r(\mathbf{k}) = \frac{\langle v_{\text{los}}^{\text{True}}(\mathbf{k}) v_{\text{los}}^{*,\text{Rec}}(\mathbf{k}) \rangle}{\langle v_{\text{los}}^{\text{True}}(\mathbf{k}) v_{\text{los}}^{*,\text{True}}(\mathbf{k}) \rangle \langle v_{\text{los}}^{\text{Rec}}(\mathbf{k}) v_{\text{los}}^{*,\text{Rec}}(\mathbf{k}) \rangle}. \quad (4.1)$$

And the correlation parameter of the clusters' LOS velocity

$$r = \frac{\langle v_{c,\text{los}}^{\text{True}} v_{c,\text{los}}^{*,\text{Rec}} \rangle}{\langle v_{c,\text{los}}^{\text{True}} v_{c,\text{los}}^{*,\text{True}} \rangle \langle v_{c,\text{los}}^{\text{Rec}} v_{c,\text{los}}^{*,\text{Rec}} \rangle}. \quad (4.2)$$

The bottom panels of figure 2 reveal the correlation function between the peculiar velocity field of dark matter particles and the reconstructed velocities in three distinct redshift bins. Notably, the correlation parameter remains high (> 0.9) at larger scales $k < 0.03 h/\text{Mpc}$ but it rapidly diminishes, approaching zero at smaller scales $k > 0.3 h/\text{Mpc}$. Furthermore, an increase in the fiducial galaxy number density by 20% yields a scale-dependent improvement in the correlation function. This improvement is minimal at $k < 0.07 h/\text{Mpc}$ and increases by about 7% for higher k value.

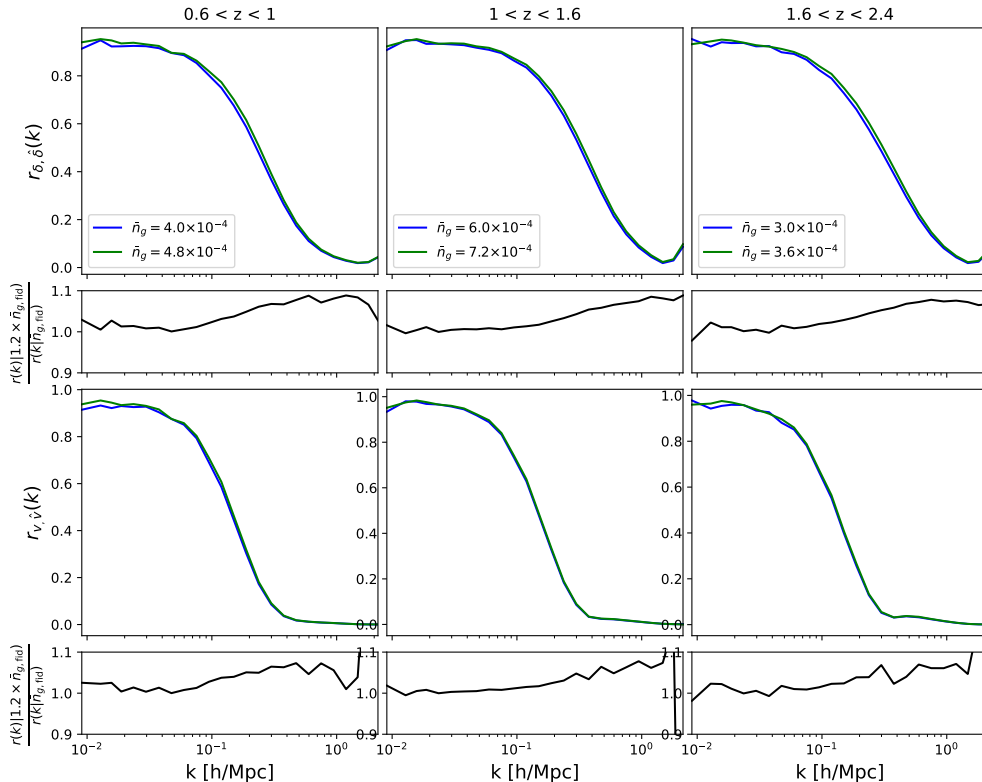


Figure 2. The correlation functions of the reconstructed density and velocity fields with the true fields from N-body simulation in three redshift bins. The first row shows the correlation function of the reconstructed density and the matter density from simulation. The blue lines represent the density reconstructed from the spectroscopic galaxy catalog with a fiducial PFS galaxy number density, while the green lines represent the density reconstruction with 20% more galaxies. The second row shows the ratio of the green and blue line, elucidating how an augmentation in galaxy number density can potentially enhance the performance of reconstruction. The third and fourth rows show the same analysis but focus on the reconstructed velocity field. For comparison, the correlation parameter between the reconstructed velocity and the true values of individual clusters is from 0.31 to 0.38, depending on the cluster mass and redshift.

4.1 Stacking method

The kSZ stacking method involves the stacking of the filtered CMB temperature signals at the position of clusters weighted by LOS velocity of clusters. The LOS velocity is reconstructed using the method outlined in section 2 and a spectroscopic redshift galaxy catalog, as described in section 3.3. This velocity-weighted stacking helps suppress the tSZ effect, dust contamination, and other foregrounds that do not correlate with the LOS velocities of the clusters.

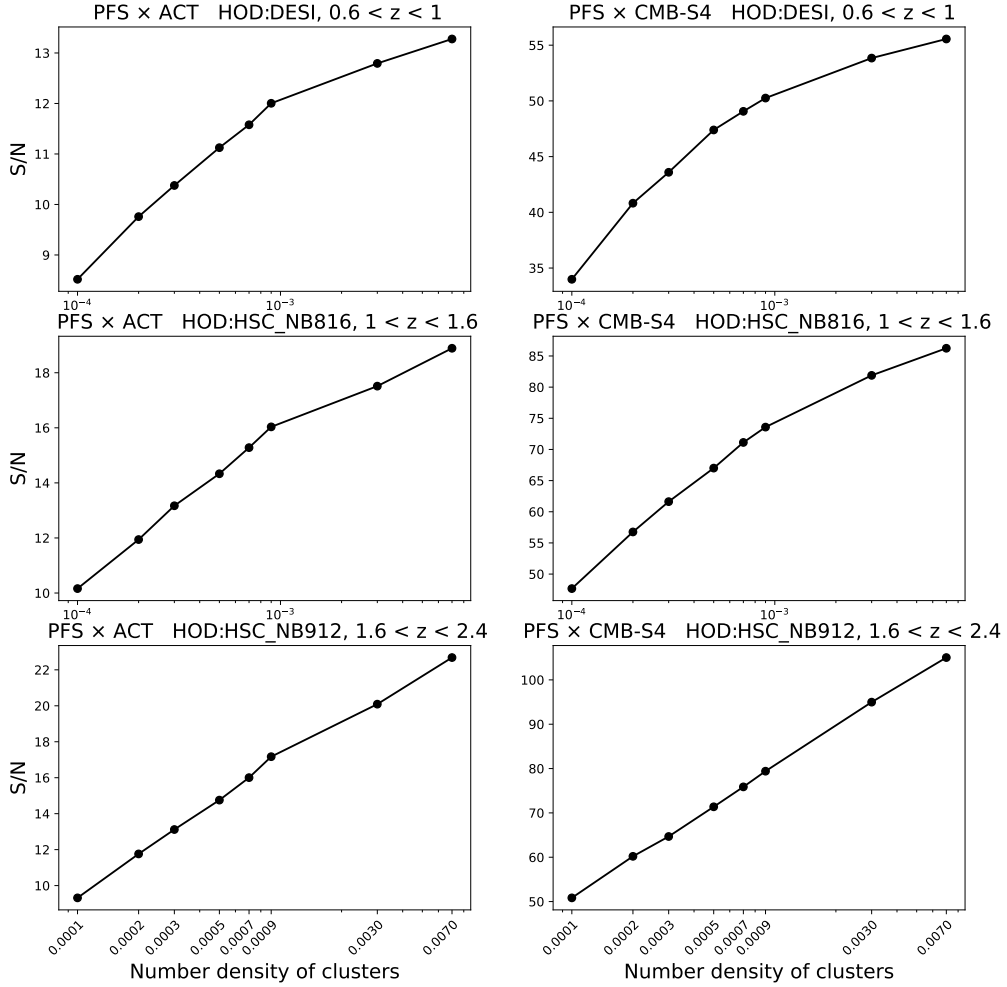


Figure 3. The measurement significance of the kSZ stacking method. The three panels from top to bottom represent the redshift bins $0.6 < z < 1.0$, $1.0 < z < 1.6$ and $1.6 < z < 2.4$ for the combination of PSF \times ACT (left) and PSF \times CMB-S4 (right).

In the first place, to suppress the instrument noise, we add a matched filter

$$W_{\text{matched}}(l) = \sqrt{\frac{C_{\text{CMB}}(l) + C_{\text{kSZ}}(l)}{C_{\text{CMB}}(l) + C_{\text{kSZ}}(l) + C_{\text{instr}}(l)}}. \quad (4.3)$$

Additionally, the amplitude of the power spectrum of the primary CMB is larger than that of the kSZ effect by more than three orders of magnitude. In larger scales, the CMB component is more dominant, and at the scale of clusters, it exhibits almost none variation. To effectively isolate the kSZ signal from the dominating CMB fluctuations, an aperture photometry (AP)

filter is applied at the location of each cluster

$$T_{\text{AP},i}(\theta_{\text{AP}}) = \int T(\vec{\theta} - \vec{\theta}_i) W_{\text{AP}}(\theta) d\vec{\theta}, \quad (4.4)$$

where $\vec{\theta}_i$ is the angular position of the cluster i . The AP filter

$$W_{\text{AP}}(\theta) = \frac{1}{\pi\theta_{\text{AP}}^2} \begin{cases} 1, & \theta \leq \theta_{\text{AP}} \\ -1, & \theta_{\text{AP}} < \theta \leq \sqrt{2}\theta_{\text{AP}} \\ 0, & \theta > \sqrt{2}\theta_{\text{AP}} \end{cases} \quad (4.5)$$

designed to be compensated, integrates over an area to zero. This feature enables the filter to cancel out fluctuations that have a wavelength longer than its size. By varying the size of the AP filter from 0.3 to 5 arcmin, it is possible to delineate the kSZ profile around clusters. The stacking estimator is

$$T_{\text{kSZ}}(\theta_{\text{AP}}) = \frac{1}{r_v} \frac{v_{\text{rec}}^{\text{rms}}}{c} \frac{\sum_i T_{\text{AP},i}(\theta_{\text{AP}})(v_{\text{rec},i}/c)}{\sum (v_{\text{rec},i}/c)^2}, \quad (4.6)$$

where $T_{\text{AP},i}(\theta_{\text{AP}})$ is the CMB temperature at the position of the cluster i after applying the AP filter whose size is θ_{AP} , $v_{\text{rec},i}$ is the reconstructed LOS velocity of the cluster i , $v_{\text{rec}}^{\text{rms}}$ is the root mean square of the reconstructed LOS velocity. And r_v is the correlation coefficient of the reconstructed and true los cluster velocity.

We use the Jackknife method [44] to estimate the precision of measurements. The cluster catalog is divided into N_{JK} subsamples. Then, we measure the observable (eq. 4.6) by removing one subsample from the dataset at a time. The Jackknife covariance is

$$C_{ij}^{\text{JK}} = \frac{N_{\text{JK}} - N_{\text{bins}} - 2}{N_{\text{JK}} - 1} \sum_k^{N_{\text{JK}}} (T_{\text{kSZ}}^k(\theta_{\text{AP},i}) - \bar{T}_{\text{kSZ}}(\theta_{\text{AP},i})) \times (T_{\text{kSZ}}^k(\theta_{\text{AP},j}) - \bar{T}_{\text{kSZ}}(\theta_{\text{AP},j})), \quad (4.7)$$

where k represents each measurement, i and j represent the i -th and j -th bin for the AP filter size, \bar{T}_{kSZ} is the mean value of N_{JK} measurements and N_{bin} is the number of the AP filter sizes.

The S/N is estimated by

$$\frac{S}{N} = \sqrt{\frac{V_{\text{survey}}}{V_{\text{simu}}}} \cdot \chi_{\text{null}}^2, \quad (4.8)$$

where V_{survey} is the comoving survey volume for the redshift bin and $V_{\text{simu}} = 1200^3 [\text{Mpc}/h]^3$ is the simulation volume, and

$$\chi_{\text{null}}^2 = \sum_{ij} \bar{T}_{\text{kSZ}}(\theta_{\text{AP},i}) (C_{ij}^{\text{JK}})^{-1} \bar{T}_{\text{kSZ}}(\theta_{\text{AP},j}). \quad (4.9)$$

Figure 3 presents our forecast of the kSZ stacking measurement significance across three redshift bins for both the ACT and CMB-S4 surveys. Notably, the CMB-S4 survey offers a significant improvement, approximately a fivefold enhancement compared to the ACT survey. This improvement arises primarily from the superior sensitivity of CMB-S4. When compared

to the ACT case, the stacking profiles from CMB-S4 exhibit a higher S/N for $\theta_{AP} < 2$ arcmin. However, the characteristic scale of clusters (~ 1 arcmin, corresponding to $l \sim 2 \times 10^4$) is dominated by instrumental noise for both ACT and CMB-S4.

Our findings further reveal a notable dependence of the S/N on cluster number density. Specifically, increasing the cluster number density within the range of 10^{-4} to 7×10^{-3} $[h/\text{Mpc}]^3$ leads to an approximate twofold increase in the S/N. Interestingly, augmenting galaxy density by 20% yielded negligible changes in measurement significance and the correlation coefficient. This aligns with the findings of ref. [25], suggesting that the reconstruction performance saturates when the galaxy number density exceeds $5 \times 10^{-5} [h/\text{Mpc}]^3$.

Furthermore, the correlation parameter between true and reconstructed cluster LOS velocity is between 0.31 to 0.38, and we observe a decreasing trend the correlation parameter with increasing cluster mass (in this case, inferred from photometric cluster redshifts). This relationship is reversed if the cluster redshift is spectroscopic instead of photometric. Notably, the LOS velocity amplitude of clusters exhibits no apparent dependence on cluster mass. We therefore conclude that the decreasing correlation for massive clusters arises from the large velocity disparity around them.

Finally, if the cluster number density could reach $1 \times 10^{-3} [h/\text{Mpc}]^3$, the S/N of the kSZ stacking method for the three redshift bins would be expected to reach 12, 17, and 18 for the ACT case and 52, 75, and 85 for the CMB-S4 case, respectively. Two primary factors influence the stacking measurements in different redshift bins: survey volume and cluster angular radius. For a fixed cluster number density, a larger survey volume translates to a higher S/N. However, at higher redshifts, the clusters with same mass will have a smaller angular radius, making it more susceptible to instrumental noise.

4.2 Tomography method

We follow the steps in ref. [30] to measure the kSZ effect by the tomography method. A kSZ template is constructed by integrating

$$\hat{\Theta}(\hat{n}) = \int_{z_1}^{z_2} W(z) \frac{\hat{\mathbf{p}}(\chi \hat{\mathbf{n}}, \chi) \cdot \hat{n}}{c} a d\chi, \quad (4.10)$$

where \hat{n} is the LOS direction, χ is the comoving distance, a is the scale factor, c is the speed of light, z is the redshift, $W(z) = \chi_e \bar{n}_e(z) \sigma_T e^{-\tau(z)}$ is the redshift weight. In the reconstructed momentum $\hat{\mathbf{p}} = \hat{\mathbf{v}} \cdot \hat{\delta}$, $\hat{\delta}$ is the galaxy density field with the weiner filter $W_2(k)$ and $\hat{\mathbf{v}}$ is the reconstructed velocity described in section 2. Then, correlate it with the CMB survey maps. The statistical error of the correlation angular power spectrum C_l is

$$\left(\frac{\Delta C_l}{C_l} \right)^2 = \frac{1}{2l\Delta l f_{\text{sky}}} \frac{(C_l^{\text{CMB}} + C_l^{\text{noise}}) C_l^{\hat{\Theta}\hat{\Theta}}}{(C_l^{\Theta\Theta})^2}, \quad (4.11)$$

where Θ is the kSZ signal $\Delta T_{\text{kSZ}}/T_{\text{CMB}}$ in this redshift bin, f_{sky} is the sky fraction, C_l^{CMB} is the angular power spectrum of the primary CMB power spectrum and C_l^{noise} is the angular power spectrum of noise. The total measurement significance of the tomography can be estimated by

$$\frac{S}{N} = \frac{1}{\sqrt{\sum (\Delta C_l / C_l)^2}}. \quad (4.12)$$

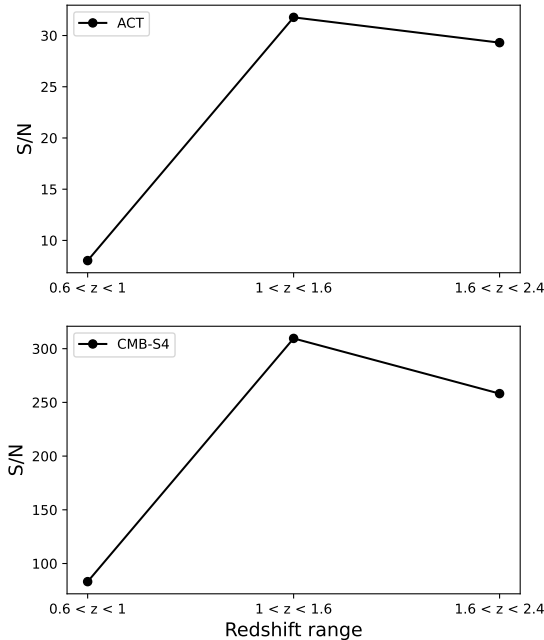


Figure 4. The measurement significance of the kSZ tomography method for the combination of PSF \times ACT (top) and PSF \times CMB-S4 (bottom). The x-axis shows the redshift range of the bins. The y-axis shows the S/N of the measurements.

Figure 4 depicts the significance of the kSZ tomography measurement, quantified by the S/N, across three redshift bins ($0.6 < z < 1$, $1 < z < 1.6$, and $1.6 < z < 2.4$) for both the ACT and CMB-S4 surveys. The S/N values for the ACT survey are 8, 32, and 28, while the CMB-S4 survey achieves significantly higher values of 80, 310, and 250, respectively. This roughly ten-fold improvement highlights the superior performance of CMB-S4 for kSZ tomography measurements.

The relatively low S/N observed for the ACT survey in the first redshift bin ($0.6 < z < 1$) suggests limitations in current CMB surveys for measuring the kSZ effect via tomography at redshifts below $z = 1$. In contrast, the S/N ratio exhibits a significant rise for both surveys in the second and the third redshift bin.

This improvement is attributed to several factors. Firstly, at higher redshifts, the comoving number density of free electrons increases, leading to a stronger kSZ signal. Secondly, larger survey volumes encompass a greater number of clusters, contributing to a higher S/N. Thirdly, for the second redshift bin, while a higher galaxy density may not significantly improve velocity reconstruction, it does contribute to a more accurate reconstruction of the underlying density field, which is crucial for tomography measurements. Fourthly, the non-linear components are reduced with the increasing of the redshift and this would also increase the reconstruction performance.

In addition, we find a 20% increase in galaxy number density is projected to improve the S/N ratio by approximately 10% across all redshift bins, underscoring the substantial impact

of galaxy density on the correlation between the kSZ signal and the reconstructed template. Incorporating complementary tracers of large-scale structure, beyond galaxy surveys alone, could potentially mitigate the impact of Poisson noise and further enhance the significance of measurements at higher redshifts.

Above all, both stacking and tomography methods in the PFS survey demonstrate powerful performance in high redshift bins. This indicates a significant potential for the PFS survey in measuring the kSZ effect at high redshifts, marking it as a key merit of this observational program. In addition, while the kSZ stacking and tomography estimators are theoretically equivalent to the bispectrum $\langle \delta\delta v \rangle$ (appendix C), they measure the 1h-term and 2h-term components respectively, like correlation function and power spectrum. Moreover, the kSZ tomography measurement only relying on PFS spectroscopic galaxy catalog possess higher S/N than that of stacking method in the two high redshift bins. This is attributed to the tomography signal capturing contributions from free electrons across various cosmic structures, including halos, filaments, and voids, whereas the stacking approach predominantly measures kSZ effects from massive clusters. Additionally, the scale region where the 1h-term dominates ($l \sim 10^4$) is severely suffered by instrumental noise, even within the CMB-S4 survey. Lastly, the kSZ tomography is more sensitive to the galaxy number density comparing to stacking method. The increasing of galaxy number density would not only improve the velocity reconstruction performance, but also the reconstructed density field itself. In addition, we find the improvement of the correlation of the reconstructed and true field show up only when $k > 0.03h/\text{Mpc}$ and slightly increase with the increasing of k (figure. 2). Therefore, the tomography method is benefit from both improvement of small scales and of reconstructed density fields.

5 Conclusion

In this study, we explore the measurement significance of applying kSZ stacking and tomography to the PFS spectroscopic redshift galaxy survey and CMB surveys like ACT and CMB-S4. Both methods involve velocity reconstruction utilizing the density field from a biased tracer, specifically the PFS spectroscopic galaxies. In the velocity reconstruction, the noise of density field caused by the RSD and shot noise should be suppressed at small scale. Compared to the Gaussian filter, our findings indicate that the optimal Wiener filter slightly enhances the correlation between the true and reconstructed velocity for $k > 0.1h/\text{Mpc}$.

To forecast the measurement significance, we use a N-body simulation to generate mock kSZ map, galaxy and group catalogs. For the kSZ mock, we assume the baryon distribution trace that of dark matter. This assumption does not account for the redistribution of baryons driven by baryonic processes. These processes, such as supernovae and AGN feedback, can expel baryonic material from clusters into the surrounding environment. This effect is likely a subdominant contributor to forecasting kSZ measurement significance and will be addressed in future discussions.

To generate the realistic PFS galaxy catalog, we employ realistic ELG HODs from a dark halo catalog. Randomly selecting galaxies ensures the galaxy number density aligns with the predicted value from PFS. Our results underscore the advantages of high redshift kSZ measurement due to its substantial signal amplitude and better velocity reconstruction performance in both methods. In the stacking method, while using the PFS galaxy sample to reconstruct velocity, we use another cluster sample to pin down where to stack kSZ temper-

ature. Interestingly, we observe that the S/N is strongly dependent on the number density of the cluster sample rather than the density of PFS galaxies. The tomography method, which only needs the PFS galaxy sample, can detect kSZ effect with the S/N = 8, 32, 28 for ACT survey and 80, 310, 250 for CMB-S4 survey respectively in the three redshift bins $0.6 < z < 1.0$, $1.0 < z < 1.6$ and $1.6 < z < 2.4$.

While the stacking method excels in measuring the detailed electron profile around massive clusters, tomography captures all free electrons in clusters, filaments, and voids, making it sensitive to the global baryon abundance. These two methods are complementary. Leveraging the PFS spectroscopic redshift survey, the kSZ measurement allows the constraint of baryon abundance extension to $z = 2.4$. Simultaneously, the kSZ measurement serves as a valuable tool to constrain baryonic process strength, offering insights into the distribution of baryons. This provides an observable means to calibrate sub-grid parameters in hydrodynamic simulations and address one of the most significant theoretical systematic uncertainties in weak lensing measurements.

Furthermore, to enhance the measurement significance beyond redshift $z = 1$, the incorporation of other high redshift data such as, the Lyman- α forest and 21cm intensity mapping, could significantly improve the reconstruction performance of peculiar velocities and redshift range. The observed increase in quasar number density facilitates more accessible and accurate density measurements through their absorption lines. But the sampling across the sky can be sparse. This characteristic poses challenges for velocity reconstruction, which we defer to future investigations.

Acknowledgments

This work made use of the Gravity Supercomputer at the Department of Astronomy, Shanghai Jiao Tong University. This work was supported by the National Key R& D Program of China (2023YFA1607800, 2023YFA1607801, 2020YFC2201602), the China Manned Space Project (#CMS-CSST-2021-A02), and the Fundamental Research Funds for the Central Universities.

A The difference between dark matter and baryon

In this study, we leverage dark matter data from N-body simulations to construct a kSZ mock. However, it is essential to acknowledge that the kSZ effect is intricately linked to the distribution and velocity of free electrons (baryons), which inherently differ from those of dark matter due to baryonic processes, such as AGN and Supernovae feedback.

This section aims to elucidate the distinctions in momentum between dark matter and baryons, employing hydrodynamic simulations from TNG100-1, a subset of the IllustrisTNG project. IllustrisTNG is a suite of state of art hydrodynamic simulations designed to explore galaxy formation and evolution in the universe. The TNG100-1 simulation incorporates 2500^3 dark matter particles and gas cells within a volume of $75^3 [\text{Mpc}/h]^3$, adopting to a cosmological model from ref. [45]. Position and velocity data for dark matter particles and gas cells are easily retrieved from the simulation, with their momentum, $\mathbf{p} = (1 + \delta)\mathbf{v}$, allocated to a grid of 512^3 . Then we calculate the power spectrum and correlation function of these two momentum fields and show them in figure 5.

In the top panel, we present the ratio of the power spectrum of baryon momentum to that of dark matter. Notably, at large scales ($k < 0.2h/ \text{Mpc}$), the ratio approaches unity

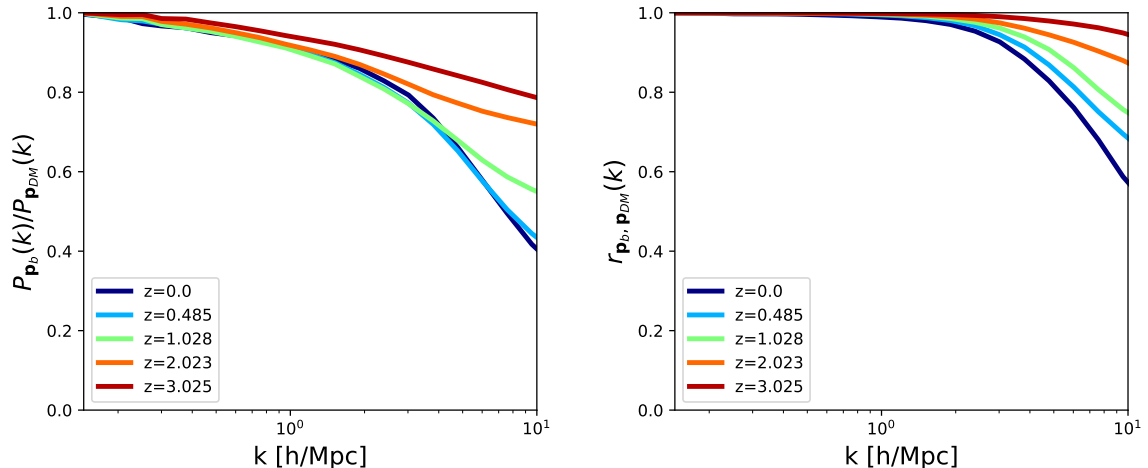


Figure 5. The ratio of baryon and dark matter momentum power spectrum (top) and the correlation function between them (bottom) from TNG100-1 simulation.

and diminishes with increasing wave number k . At $k = 1h/ \text{Mpc}$, the ratio remains above 0.9 for all redshifts. The bottom panel illustrates the correlation function between dark matter and baryon momentum, demonstrating near unity correlation at scales $k < 1h/ \text{Mpc}$ for all redshifts, with a decrease as k increases. Furthermore, both the ratio and correlation tend towards unity when $k < 1h/ \text{Mpc}$, indicating diminished differences between dark matter and baryons, especially at higher redshifts. Although, in the main body of our analysis, we assume that the distribution and velocity of baryons mimic those of dark matter. We acknowledge this assumption may cause potential bias in kSZ mock, particularly at lower redshifts and smaller scales. However, for the redshift and scale range of our interest, this bias is expected to have a negligible impact on the estimation of kSZ measurement significance.

B Connection between halos and galaxies

The CosmicGrowth is a dark-matter simulation which only contain halos and subhalos. In this work, we use the ELG sample from PFS to reconstruct the velocity field. The ELG is a type of galaxy characterized by their strong emission lines in their spectra. These emission lines are typically caused by gas within the galaxy being excited by young, hot stars or AGNs. ELGs often exhibit high levels of star formation activity. They are not necessary to be bright reside in the massive halos. We employ three kinds of ELG HOD to sample the galaxies into the halos. The first is from [41]. They use the galaxy catalog of the final public release of the VIPERS and a photometric catalog from Canada-France-Hawaii Telescope Legacy Survey. They choose the galaxy sample in the redshift range $0.5 \leq z \leq 0.8$ and divide the galaxies into four luminosity bins, and fit the HOD for each bin. The HOD model formula they used

Redshift bin	Sample	$\log M_c$	$\sigma_{\log M}$	F_c^A	F_c^B	β_c	$\log M_{\min}$	F_s	$\delta_{\log M}$	α_s
$0.6 \leq z \leq 1.0$	L0	11.234	0.206	0.133	0.010	-0.185	11.690	0.015	0.516	0.947
	L1	11.415	0.224	0.091	0.146	-0.187	11.668	0.012	0.516	0.939
	L2	11.528	0.241	0.035	0.075	-0.168	11.723	0.005	0.508	0.940
	L3	11.558	0.217	0.010	0.021	-0.065	11.783	0.001	0.492	0.950
$1.0 \leq z \leq 1.6$	NB816	11.75	0.06	0.13	0.95	-	12.46	0.98	1	1.06
$1.6 \leq z \leq 2.4$	NB912	11.93	0.13	0.14	0.90	-	12.46	0.98	1	1.06

Table 2. The value of the HOD parameters in eq. B.1. The first column shows in which redshift we used these HOD models, note it is not the same with the redshift range of the galaxy sample to fit these parameters. The first four rows shows the fitting result in Table 4 of ref. [41]. And the last two rows shows the fitting results in Table 3 of ref. [10].

is

$$N_{\text{cen}}(M) = F_c^B (1 - F_c^A) \exp \left[-\frac{(\log(M/M_c))^2}{2\sigma_{\log M}^2} \right] \quad (\text{B.1})$$

$$+ F_c^A \left[1 + \text{erf} \left(\frac{\log(M/M_c)}{\sigma_{\log M}} \right) \right] \times \left(1 + \frac{M}{M_c} \right)^{\beta_c}$$

$$N_{\text{sat}}(M) = F_s \left[1 + \text{erf} \left(\frac{\log(M/M_{\min})}{\delta_{\log M}} \right) \right] \times \left(\frac{M}{M_{\min}} \right)^{\alpha_s}. \quad (\text{B.2})$$

We used this HOD to sample the galaxy at the redshift range 0.6–1 in the main text. And the second is from [46], which use the the ELGs identified by two narrow-band, NB816 ($z=1.19$) and NB912 ($z=1.47$), in the HSC-SSP survey. They used the same HOD model formula with the first one, but $\beta_s = 0$ We use these two HODs for the redshift range 1.0 ~ 1.6 and 1.6 ~ 2.4 respectively. The value of the parameters in these HODs are listed in the table B.

C The equivalence between kSZ measurement methods

The essence of measuring kSZ effect by cross-correlating a CMB and density survey is a bispectrum of temperature, large scale velocity (equivalent to density) and density, $\langle T\delta\delta \rangle$. [47] has shown that the different methods of kSZ measurement are equivalent to each other formulaically. This section will briefly show the demonstration following the steps in [47]. The starting is from the most general form of a three-point estimator

$$\hat{\xi} = \int \frac{d^3\mathbf{k}}{(2\pi)^3} \frac{d^3\mathbf{k}'}{(2\pi)^3} \frac{d^2\mathbf{l}}{(2\pi)^2} W(\mathbf{k}, \mathbf{k}', \mathbf{l}) (\delta_g(\mathbf{k})\delta_g(\mathbf{k}')T(\mathbf{l}))$$

$$(2\pi)^3 \delta^3(\mathbf{k} + \mathbf{k}' + \frac{\mathbf{l}}{\chi_*}). \quad (\text{C.1})$$

Next step is to determine the weighting function $W(\mathbf{k}, \mathbf{k}', \mathbf{l})$, by minimizing the variance of $\hat{\xi}$. Requiring the estimator to be unbiased, the weight function would be

$$W(\mathbf{k}, \mathbf{k}', \mathbf{l}) = \frac{1}{2F_{BB}} \frac{-iB^*(k, k', l, k_r)}{P_{gg}^{\text{tot}}(k)P_{gg}^{\text{tot}}(k')C_l^{TT, \text{tot}}}, \quad (\text{C.2})$$

where F_{BB} is the fisher matrix, $P_{gg}^{\text{tot}}(k)$ is the total power spectrum of the galaxies, $C_l^{TT, \text{tot}}$ is the power spectrum of CMB including the instrument noise, and $B(k, k', l, k_r)$ is the

bispectrum

$$\langle \delta_g(\mathbf{k}) \delta_g(\mathbf{k}') T(\mathbf{l}) \rangle = B(\mathbf{k}, \mathbf{k}', \mathbf{l}) (2\pi)^3 \delta^3 \left(\mathbf{k} + \mathbf{k}' + \frac{\mathbf{l}}{\chi_*} \right). \quad (\text{C.3})$$

It can be inferred that in the "squeezed" limit (k is small, while k' and l are large), the tree-level kSZ bispectrum, which is assumed to be an accurate approximation of the kSZ bispectrum, is

$$B(k_L, k_S, l, k_{Lr}) = -\frac{K_* k_{Lr}}{\chi_*^2} \frac{P_{gv}(k_L)}{k_L} P_{ge}(k_S) \quad (\text{C.4})$$

Then the estimator becomes

$$\begin{aligned} \hat{\mathcal{E}} &= \frac{K_*}{\chi_*^2 F_{BB}} \int \frac{d^3 \mathbf{k}_L}{(2\pi)^3} \frac{d^3 \mathbf{k}_S}{(2\pi)^3} \frac{d^2 \mathbf{l}}{(2\pi)^2} \frac{ik_{Lr}}{k_L} \\ &\quad \frac{P_{gv}(k_L) P_{ge}(k_S)}{P_{gg}^{\text{tot}}(k_L) P_{gg}^{\text{tot}}(k_S) C_l^{TT, \text{tot}}} \\ &\quad (\delta_g(\mathbf{k}_L) \delta_g(\mathbf{k}_S) T(\mathbf{l})) (2\pi)^3 \delta^3 \left(\mathbf{k}_L + \mathbf{k}_S + \frac{\mathbf{l}}{\chi_*} \right) \end{aligned} \quad (\text{C.5})$$

- **Prove stacking method is equivalent to the estimator**

At the positions of galaxies, the velocity weighted stacking temperature is

$$\hat{\alpha} = \sum_i \hat{v}_i \tilde{T}_i, \quad (\text{C.6})$$

where \hat{v}_i is the reconstructed LOS velocity \tilde{T}_i is the filtered CMB temperature at position of galaxy i . The estimator (eq. C.5) can be rewritten with $\delta_g(\mathbf{k}_S) = \frac{1}{\bar{n}_g} \sum_i e^{-i\mathbf{k}_S \cdot \mathbf{x}_i}$ as

$$\begin{aligned} \hat{\mathcal{E}} &= \frac{1}{\bar{n}_g} \sum_i \left(\int \frac{d^3 \mathbf{k}_L}{(2\pi)^3} \frac{ik_{Lr}}{k_L} \frac{P_{gv}(k_L)}{P_{gg}^{\text{tot}}(k_L)} \delta_g(\mathbf{k}_L) e^{-i\mathbf{k}_L \cdot \mathbf{x}_i} \right) \\ &\quad \times \left(\int \frac{d^2 \mathbf{l}}{(2\pi)^2} \frac{P_{ge}(l/\chi_*)}{P_{gg}^{\text{tot}}(l/\chi_*) C_l^{TT, \text{tot}}} T(\mathbf{l}) e^{-i\mathbf{l} \cdot \mathbf{x}_i^\perp / \chi_*} \right) \end{aligned} \quad (\text{C.7})$$

The normalization $K_*/\chi_*^2 F_{BB}$ is removed for simplicity. Then the reconstructed velocity and the filtered temperature can be represented as

$$\hat{v}_i = \int \frac{d^3 \mathbf{k}_L}{(2\pi)^3} \frac{ik_{Lr}}{k_L} \frac{P_{gv}(k_L)}{P_{gg}^{\text{tot}}(k_L)} \delta_g(\mathbf{k}_L) e^{-i\mathbf{k}_L \cdot \mathbf{x}_i} \quad (\text{C.8})$$

$$\tilde{T}_i = \int \frac{d^2 \mathbf{l}}{(2\pi)^2} \frac{P_{ge}(l/\chi_*)}{P_{gg}^{\text{tot}}(l/\chi_*) C_l^{TT, \text{tot}}} T(\mathbf{l}) e^{-i\mathbf{l} \cdot \mathbf{x}_i^\perp / \chi_*}. \quad (\text{C.9})$$

In addition, the above equations also point out the optimal filter for the reconstructed velocity and the filtered temperature.

- **Prove tomography method is equivalent to the estimator**

The kSZ tomography template is the product of the reconstructed velocity and density along the line of sight

$$\hat{\Theta} = \int_{z_1}^{z_2} dz \hat{v} \hat{\delta}, \quad (\text{C.10})$$

where

$$\hat{v} = \frac{ik_{Lr}}{k_L} \frac{P_{gv}(k_L)}{P_{gg}^{\text{tot}}(k_L)} \delta_g(\mathbf{k}_L) \quad (\text{C.11})$$

$$\hat{\delta} = \frac{P_{ge}(k_S)}{P_{gg}^{\text{tot}}(k_S)} \delta_g(\mathbf{k}_S) \quad (\text{C.12})$$

Here,

$$W_1 = \frac{P_{gv}(k_L)}{P_{gg}^{\text{tot}}(k_L)} \quad (\text{C.13})$$

$$W_2 = \frac{P_{ge}(k_S)}{P_{gg}^{\text{tot}}(k_S)} \quad (\text{C.14})$$

are the optimal filters to reconstruct \hat{v} and $\hat{\delta}$. The template $\hat{\Theta}$ in Fourier space is

$$\begin{aligned} \hat{T}(\mathbf{l}) = & \int \frac{d^3\mathbf{k}_L}{(2\pi)^3} \frac{d^3\mathbf{k}_S}{(2\pi)^3} \frac{ik_{Lr}}{k_L} \frac{P_{gv}(k_L)}{P_{gg}^{\text{tot}}(k_L)} \frac{P_{ge}(k_S)}{P_{gg}^{\text{tot}}(k_S)} \\ & (\delta_g(\mathbf{k}_L) \delta_g(\mathbf{k}_S)) (2\pi)^3 \delta^3 \left(\mathbf{k}_L + \mathbf{k}_S - \frac{\mathbf{l}}{\chi^*} \right) \end{aligned} \quad (\text{C.15})$$

And the estimator becomes to

$$\hat{\mathcal{E}} = \int \frac{d^2\mathbf{l}}{(2\pi)^2} \frac{1}{C_l^{TT,\text{tot}}} (T(\mathbf{l})T(-\mathbf{l})), \quad (\text{C.16})$$

where $T(\mathbf{l})T(-\mathbf{l})$ is the correlation between the template $\hat{\Theta}$ and the true kSZ signal Θ .

D Test the velocity reconstruction method

In this section, our research delves into the impact of applying different filters to the density field on velocity reconstruction performance. In the previous literatures, Gaussian filters in Fourier space, represented as $W_g(k) = \exp(-k^2 R_s^2)$, have been utilized to mitigate shot noise in galaxy density fields, with R_s being a pivotal, adjustable parameter for optimizing velocity reconstruction. In figure 6, we present a comparative analysis of the correlation coefficients across various mass bins of clusters and the correlation function between true and reconstructed velocities. Our findings suggest that, in the stacking method, the performance of the optimal Gaussian filter is comparable to the Wiener filter discussed in the main text. However, the Wiener filter demonstrates a noticeable advantage in the tomography method at smaller scales $k > 0.1[h/\text{Mpc}]$, highlighting the Wiener filter's efficacy in enhancing velocity reconstruction at these scales.

References

- [1] M. Fukugita and P.J.E. Peebles, *The Cosmic Energy Inventory*, *Astrophysical Journal* **616** (2004) 643 [[astro-ph/0406095](#)].
- [2] J.N. Bregman, *The Search for the Missing Baryons at Low Redshift*, *Annual Review of Astronomy and Astrophysics* **45** (2007) 221 [[0706.1787](#)].

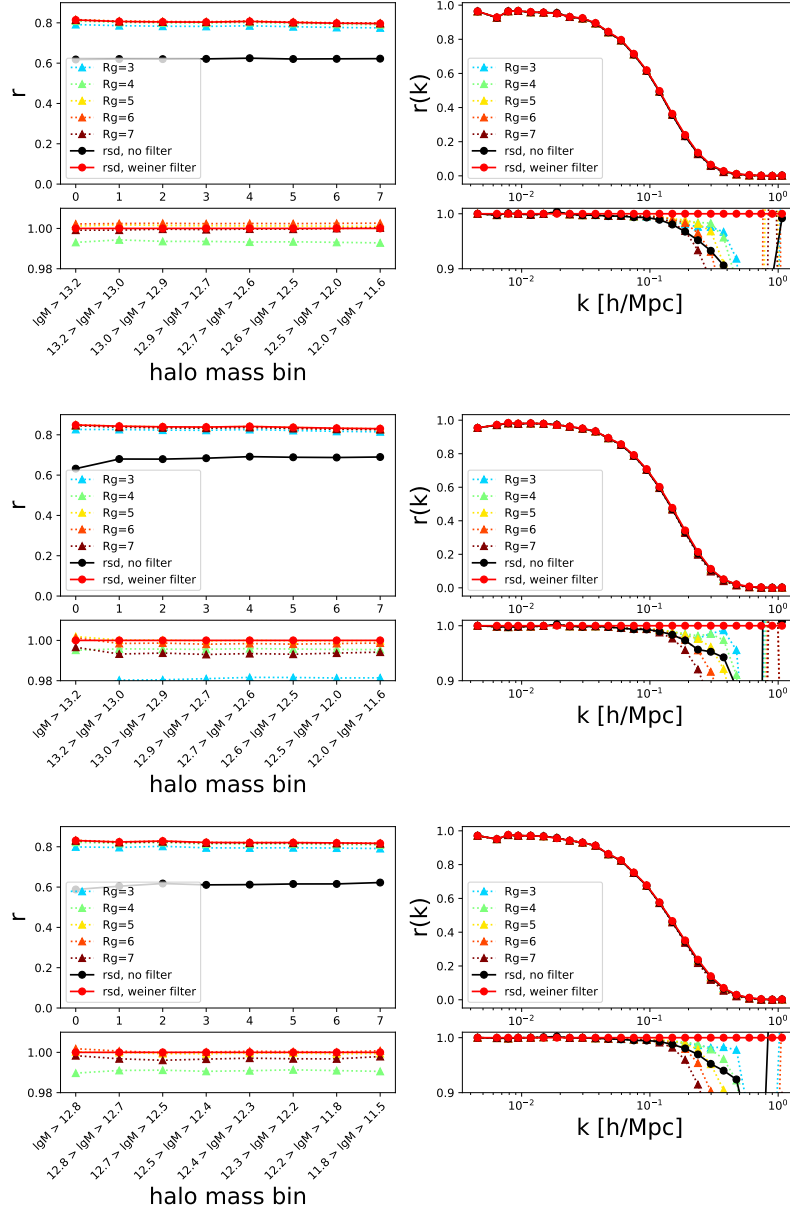


Figure 6. The correlation coefficient of different cluster mass bins (left) and the correlation function (right) of the true and reconstructed velocity fields in three redshift bins $0.6 < z < 1.0$, $1.0 < z < 1.6$ and $1.6 < z < 2.4$ (from top to bottom). The black lines show the case that reconstructing velocity field directly from δ_g without applying any filters. The red lines show the case of applying the Wiener filter using the main text. The dashes lines show the case of applying the Gaussian filter with different radius R_g .

- [3] N. Battaglia, *The Tau of Galaxy Clusters*, *Journal of Cosmology and Astroparticle Physics* **2016** (2016) 058 [[1607.02442](#)].
- [4] M.S. Madhavacheril, N. Battaglia, K.M. Smith and J.L. Sievers, *Cosmology with kSZ: Breaking the optical depth degeneracy with Fast Radio Bursts*, *Physical Review D* **100** (2019) 103532 [[1901.02418](#)].
- [5] P. Collaboration, P.A.R. Ade, N. Aghanim, M. Arnaud, M. Ashdown, J. Aumont et al., *Planck intermediate results. XIII. Constraints on peculiar velocities*, *Astronomy & Astrophysics* **561** (2014) A97 [[1303.5090](#)].
- [6] D. Alonso, T. Louis, P. Bull and P.G. Ferreira, *Reconstructing cosmic growth with kSZ observations in the era of Stage IV experiments*, *Physical Review D* **94** (2016) 043522 [[1604.01382](#)].
- [7] E.-M. Mueller, F. de Bernardis, R. Bean and M. Niemack, *Constraints on gravity and dark energy from the pairwise kinematic Sunyaev-Zeldovich effect*, *The Astrophysical Journal* **808** (2015) 47 [[1408.6248](#)].
- [8] F. Bianchini and A. Silvestri, *Kinetic Sunyaev-Zeldovich effect in modified gravity*, *Physical Review D* **93** (2016) 064026 [[1510.08844](#)].
- [9] M.A. Mitchell, C. Arnold, C. Hernández-Aguayo and B. Li, *The impact of modified gravity on the Sunyaev-Zel'dovich effect*, *Monthly Notices of the Royal Astronomical Society* **501** (2021) 4565 [[2011.00013](#)].
- [10] T. Okumura and A. Taruya, *Tightening geometric and dynamical constraints on dark energy and gravity: Galaxy clustering, intrinsic alignment and kinetic Sunyaev-Zel'dovich effect*, *Physical Review D* **106** (2022) 043523 [[2110.11127](#)].
- [11] E.-M. Mueller, F. de Bernardis, R. Bean and M.D. Niemack, *Constraints on massive neutrinos from the pairwise kinematic Sunyaev-Zel'dovich effect*, *Physical Review D* **92** (2015) 063501 [[1412.0592](#)].
- [12] N. Hand, G.E. Addison, E. Aubourg, N. Battaglia, E.S. Battistelli, D. Bizyaev et al., *Evidence of Galaxy Cluster Motions with the Kinematic Sunyaev-Zel'dovich Effect*, *Physical Review Letters* **109** (2012) 041101 [[1203.4219](#)].
- [13] Planck Collaboration, P.A.R. Ade, N. Aghanim, M. Arnaud, M. Ashdown, E. Aubourg et al., *Planck intermediate results. XXXVII. Evidence of unbound gas from the kinetic Sunyaev-Zeldovich effect*, *Astronomy & Astrophysics* **586** (2016) A140 [[1504.03339](#)].
- [14] F. De Bernardis, S. Aiola, E.M. Vavagiakis, N. Battaglia, M.D. Niemack, J. Beall et al., *Detection of the pairwise kinematic Sunyaev-Zel'dovich effect with BOSS DR11 and the Atacama Cosmology Telescope*, *Journal of Cosmology and Astroparticle Physics* **2017** (2017) 008 [[1607.02139](#)].
- [15] Y.-C. Li, Y.-Z. Ma, M. Remazeilles and K. Moodley, *Measurement of the pairwise kinematic Sunyaev-Zeldovich effect with Planck and BOSS data*, *Physical Review D* **97** (2018) 023514 [[1710.10876](#)].
- [16] V. Calafut, P.A. Gallardo, E.M. Vavagiakis, S. Amodeo, S. Aiola, J.E. Austermann et al., *The Atacama Cosmology Telescope: Detection of the Pairwise Kinematic Sunyaev-Zel'dovich Effect with SDSS DR15 Galaxies*, *Physical Review D* **104** (2021) 043502 [[2101.08374](#)].
- [17] B. Soergel, S. Flender, K.T. Story, L. Bleem, T. Giannantonio, G. Efstathiou et al., *Detection of the kinematic Sunyaev-Zel'dovich effect with DES Year 1 and SPT*, *Monthly Notices of the Royal Astronomical Society* **461** (2016) 3172 [[1603.03904](#)].
- [18] Z. Chen, P. Zhang, X. Yang and Y. Zheng, *Detection of pairwise kSZ effect with DESI galaxy clusters and Planck*, *Monthly Notices of the Royal Astronomical Society* **510** (2022) 5916 [[2109.04092](#)].

- [19] E. Schiappucci, F. Bianchini, M. Aguena, M. Archipley, L. Balkenhol, L.E. Bleem et al., *A measurement of the mean central optical depth of galaxy clusters via the pairwise kinematic Sunyaev-Zel'dovich effect with SPT-3G and DES*, *Physical Review D* **107** (2023) 042004 [2207.11937].
- [20] S. Li, Y. Zheng, Z. Chen, H. Xu and X. Yang, *Detection of pairwise kSZ effect with DESI galaxy groups and Planck in Fourier space*, *arXiv e-prints* (2024) arXiv:2401.03507 [2401.03507].
- [21] M. Li, R.E. Angulo, S.D.M. White and J. Jasche, *Matched filter optimization of kSZ measurements with a reconstructed cosmological flow field*, *Monthly Notices of the Royal Astronomical Society* **443** (2014) 2311 [1404.0007].
- [22] E. Schaan, S. Ferraro, M. Vargas-Magaña, K.M. Smith, S. Ho, S. Aiola et al., *Evidence for the kinematic Sunyaev-Zel'dovich effect with ACTPol and velocity reconstruction from BOSS*, *Physical Review D* **93** (2016) 082002 [1510.06442].
- [23] E. Schaan, S. Ferraro, S. Amodeo, N. Battaglia, S. Aiola, J.E. Austermann et al., *The Atacama Cosmology Telescope: Combined kinematic and thermal Sunyaev-Zel'dovich measurements from BOSS CMASS and LOWZ halos*, *Physical Review D* **103** (2021) 063513 [2009.05557].
- [24] M. Mallaby-Kay, S. Amodeo, J.C. Hill, M. Aguena, S. Allam, O. Alves et al., *The Kinematic Sunyaev-Zel'dovich Effect with ACT, DES, and BOSS: A Novel Hybrid Estimator*, *Physical Review D* **108** (2023) 023516 [2305.06792].
- [25] B.R. Guachalla, E. Schaan, B. Hadzhiyska and S. Ferraro, *Velocity reconstruction in the era of DESI and Rubin (part I): Exploring spectroscopic, photometric & hybrid samples*, Dec., 2023.
- [26] B. Hadzhiyska, S. Ferraro, B.R. Guachalla and E. Schaan, *Velocity reconstruction in the era of DESI and Rubin (part II): Realistic samples on the light cone*, Dec., 2023.
- [27] H. Tanimura, N. Aghanim, V. Bonjean and S. Zaroubi, *Convolutional Neural Network-reconstructed velocity for kinetic SZ detection*, *Astronomy & Astrophysics* **662** (2022) A48 [2201.01643].
- [28] H. Tanimura, S. Zaroubi and N. Aghanim, *Direct detection of the kinetic Sunyaev-Zel'dovich effect in galaxy clusters*, *Astronomy & Astrophysics* **645** (2021) A112 [2007.02952].
- [29] S. Ho, S. Dedeo and D. Spergel, *Finding the Missing Baryons Using CMB as a Backlight*, Mar., 2009.
- [30] J. Shao, P. Zhang, W. Lin, Y. Jing and J. Pan, *The kinetic SZ tomography with spectroscopic redshift surveys*, *Monthly Notices of the Royal Astronomical Society* **413** (2011) 628 [1004.1301].
- [31] C. Hernández-Monteagudo, Y.-z. Ma, F.-S. Kitaura, W. Wang, R. Génova-Santos, J. Macías-Pérez et al., *Constraints on the missing baryons from the kinetic Sunyaev-Zeldovich effect in Planck data*, *Physical Review Letters* **115** (2015) 191301 [1504.04011].
- [32] J.C. Hill, S. Ferraro, N. Battaglia, J. Liu and D.N. Spergel, *The Kinematic Sunyaev-Zel'dovich Effect with Projected Fields: A Novel Probe of the Baryon Distribution with Planck, WMAP, and WISE Data*, *Physical Review Letters* **117** (2016) 051301 [1603.01608].
- [33] A. Kusiak, B. Bolliet, S. Ferraro, J.C. Hill and A. Krolewski, *Constraining the Baryon Abundance with the Kinematic Sunyaev-Zel'dovich Effect: Projected-Field Detection Using Planck, WMAP, and unWISE*, *Physical Review D* **104** (2021) 043518 [2102.01068].
- [34] N.S. Sugiyama, T. Okumura and D.N. Spergel, *A direct measure of free electron gas via the Kinematic Sunyaev-Zel'dovich effect in Fourier-space analysis*, *Monthly Notices of the Royal Astronomical Society* **475** (2018) 3764 [1705.07449].
- [35] S. Lim, H.J. Mo, H. Wang and X. Yang, *Detection of missing baryons in galaxy groups with kinetic Sunyaev-Zel'dovich effect*, *The Astrophysical Journal* **889** (2020) 48 [1912.10152].

- [36] X. Yang, H.J. Mo, F.C. van den Bosch, A. Pasquali, C. Li and M. Barden, *Galaxy Groups in the SDSS DR4. I. The Catalog and Basic Properties*, *Astrophysical Journal* **671** (2007) 153 [[0707.4640](#)].
- [37] S. Amodeo, N. Battaglia, E. Schaan, S. Ferraro, E. Moser, S. Aiola et al., *The Atacama Cosmology Telescope: Modeling the Gas Thermodynamics in BOSS CMASS galaxies from Kinematic and Thermal Sunyaev-Zel'dovich Measurements*, *Physical Review D* **103** (2021) 063514 [[2009.05558](#)].
- [38] Y. Zheng and P. Zhang, *Forecast constraints on the baryonic feedback effect from the future kinetic Sunyaev-Zel'dovich effect detection*, *arXiv e-prints* (2024) arXiv:2401.03510 [[2401.03510](#)].
- [39] Z. Chen, D. Jamieson, E. Komatsu, S. Bose, K. Dolag, B. Hadzhiyska et al., *Statistics of thermal gas pressure as a probe of cosmology and galaxy formation*, *arXiv e-prints* (2023) arXiv:2309.16323 [[2309.16323](#)].
- [40] M. Takada, R.S. Ellis, M. Chiba, J.E. Greene, H. Aihara, N. Arimoto et al., *Extragalactic science, cosmology, and Galactic archaeology with the Subaru Prime Focus Spectrograph*, *Publications of the Astronomical Society of Japan* **66** (2014) R1 [[1206.0737](#)].
- [41] H. Gao, Y.P. Jing, Y. Zheng and K. Xu, *Constructing the Emission-line Galaxy-Host Halo Connection through Auto and Cross Correlations*, *Astrophysical Journal* **928** (2022) 10 [[2111.11657](#)].
- [42] Y. Jing, *CosmicGrowth Simulations—Cosmological simulations for structure growth studies*, *Science China Physics, Mechanics, and Astronomy* **62** (2019) 19511 [[1807.06802](#)].
- [43] A. Lewis, A. Challinor and A. Lasenby, *Efficient Computation of Cosmic Microwave Background Anisotropies in Closed Friedmann-Robertson-Walker Models*, *Astrophysical Journal* **538** (2000) 473 [[astro-ph/9911177](#)].
- [44] J. Hartlap, P. Simon and P. Schneider, *Why your model parameter confidences might be too optimistic. Unbiased estimation of the inverse covariance matrix*, *Astronomy & Astrophysics* **464** (2007) 399 [[astro-ph/0608064](#)].
- [45] Planck Collaboration, P.A.R. Ade, N. Aghanim, M. Arnaud, M. Ashdown, J. Aumont et al., *Planck 2015 results. XIII. Cosmological parameters*, *Astronomy & Astrophysics* **594** (2016) A13 [[1502.01589](#)].
- [46] T. Okumura, M. Hayashi, I.N. Chiu, Y.-T. Lin, K. Osato, B.-C. Hsieh et al., *Angular clustering and host halo properties of [O II] emitters at $z \lesssim 1$ in the Subaru HSC survey*, *Publications of the Astronomical Society of Japan* **73** (2021) 1186 [[2012.12224](#)].
- [47] K.M. Smith, M.S. Madhavacheril, M. Münchmeyer, S. Ferraro, U. Giri and M.C. Johnson, *KSZ tomography and the bispectrum*, Oct., 2018.